Article

The ^{13}CO-rich atmosphere of a young accreting super-Jupiter

Yapeng Zhang[1], Ignas A. G. Snellen[1✉], Alexander J. Bohn[1], Paul Mollière[2], Christian Ginski[3], H. Jens Hoeijmakers[4,5], Matthew A. Kenworthy[1], Eric E. Mamajek[6,7], Tiffany Meshkat[8], Maddalena Reggiani[9] & Frans Snik[1]

Isotope abundance ratios have an important role in astronomy and planetary sciences, providing insights into the origin and evolution of the Solar System, interstellar chemistry and stellar nucleosynthesis[1,2]. In contrast to deuterium/hydrogen ratios, carbon isotope ratios are found to be roughly constant (around 89) in the Solar System[1,3], but do vary on galactic scales with a ^{12}C/^{13}C isotopologue ratio of around 68 in the current local interstellar medium[4–6]. In molecular clouds and protoplanetary disks, ^{12}CO/^{13}CO ratios can be altered by ice and gas partitioning[7], low-temperature isotopic ion-exchange reactions[8] and isotope-selective photodissociation[9]. Here we report observations of ^{13}CO in the atmosphere of the young, accreting super-Jupiter TYC 8998-760-1 b, at a statistical significance of more than six sigma. Marginalizing over the planet's atmospheric temperature structure, chemical composition and spectral calibration uncertainties suggests a ^{12}CO/^{13}CO ratio of 31^{+17}_{-10} (90% confidence), a substantial enrichment in ^{13}C with respect to the terrestrial standard and the local interstellar value. As the current location of TYC 8998-760-1 b at greater than or equal to 160 astronomical units is far beyond the CO snowline, we postulate that it accreted a substantial fraction of its carbon from ices enriched in ^{13}C through fractionation.

TYC 8998-760-1 b (hereafter TYC 8998 b)[10] is a widely separated planetary mass companion around a young solar analogue TYC 8998-760-1 (also known as 2MASS J13251211−6456207) with an age of about 17 Myr (ref. [11]). With the recent detection of a second planet[12], it is part of the first directly imaged multiplanet system around a solar-type star. TYC 8998 b is located at a projected separation of 160 AU, with an estimated mass of $14 \pm 3\ M_J$. We observed the planet on two nights, 5 and 19 June 2019, using Spectrograph for Integral Field Observations in the Near Infrared (SINFONI)[13,14] installed at the Cassegrain focus of Unit Telescope 3 (UT3) of the Very Large Telescope of the European Southern Observatory at Cerro Paranal, Chile. The observations were performed in the K-band (1.95–2.45 μm), providing a spectral resolving power of about $R = 4,500$. We extracted the spectrum of TYC 8998 b from 2.10 μm to 2.45 μm, as detailed in Methods.

As shown in Fig. 1, the planet spectrum is dominated by molecular features from water (H_2O) and carbon monoxide (CO). The ^{12}CO bandheads of the vibrational transitions $v = 2–0$, $v = 3–1$ and $v = 4–2$ bandheads are visible at 2.2935 μm, 2.3227 μm and 2.3535 μm, respectively. When we compare the observed spectrum with the best-fit model obtained by atmospheric retrieval, an extra emission signature at 2.166 μm is seen in Fig. 1c, which is identified as the hydrogen Brackett γ (Brγ) recombination line. This is probably an indication of ongoing accretion of circumplanetary material onto the planet. We estimated a mass accretion rate of $10^{-9.4\pm1.3}\ M_\odot\ yr^{-1}$ using the Brγ line luminosity (Methods). Future observations at longer wavelengths and

polarimetric data can provide further insights into the circumplanetary disk and accretion process[15].

To characterize the atmosphere of the planet, we performed a Bayesian retrieval analysis on the spectrum using the radiative transfer tool petitRADTRANS (pRT)[16], connected to the nested sampling tool PyMultiNest[17]. We focus on revealing the presence of ^{13}CO, which is expected to be the most detectable isotopologue in the atmospheres of gas giants[18], and measuring the isotopologue abundance ratio ^{12}CO/^{13}CO. In addition, we aim to constrain atmospheric properties of the planet, such as the carbon-to-oxygen ratio C/O, which may shed light on the conditions during the formation of the planet[19].

We set up the retrieval model in a similar way as used in previous work on HR 8799 e (ref. [20]; Methods). The model consists of nine free parameters: the planet radius R_P, surface gravity $\log g$, metallicity [Fe/H], the carbon-to-oxygen ratio C/O, the isotopologue abundance ratio ^{12}CO/^{13}CO, three parameters for the temperature–pressure (T–P) profile and a spectral slope correction factor f_{slope}, arising from uncertainties in the calibration of the observed spectrum. We ran retrievals on the spectrum of TYC 8998 b using two sets of models: the full model including ^{13}CO and the reduced model excluding ^{13}CO. The setups of the two models are identical, except that we removed ^{13}CO from the opacity sources (and therefore the ^{12}CO/^{13}CO parameter) in the reduced model. The best-fit model spectra are compared with the observed spectrum shown in Fig. 1. The difference between the two models is visible at the ^{13}CO bandheads around 2.345 μm (Fig. 1b). The full model provides a

[1]Leiden Observatory, Leiden University, Leiden, The Netherlands. [2]Max-Planck-Institut für Astronomie, Heidelberg, Germany. [3]Anton Pannekoek Institute for Astronomy, University of Amsterdam, Amsterdam, The Netherlands. [4]Observatoire de Genève, Université de Genève, Versoix, Switzerland. [5]Lund Observatory, Department of Astronomy and Theoretical Physics, Lunds Universitet, Lund, Sweden. [6]Jet Propulsion Laboratory, California Institute of Technology, Pasadena, CA, USA. [7]Department of Physics and Astronomy, University of Rochester, Rochester, NY, USA. [8]IPAC, California Institute of Technology, Pasadena, CA, USA. [9]Institute of Astronomy, KU Leuven, Leuven, Belgium. ✉e-mail: snellen@strw.leidenuniv.nl
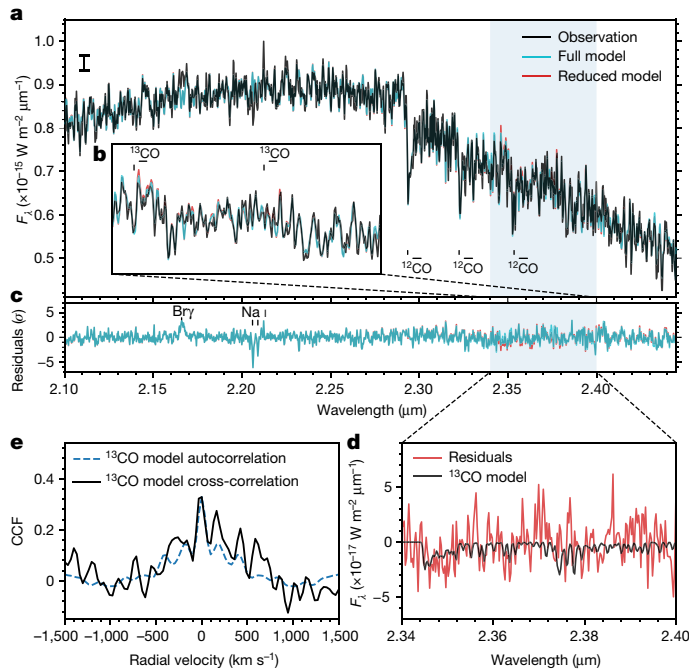
Fig. 1 | Observed SINFONI spectrum of exoplanet TYC 8998 b and cross-correlation signal of ^{13}CO. a, The observed spectrum (flux density, F_λ) is shown in black, the best-fit model including all carbon isotopes is shown in cyan and the best-fit reduced model, without ^{13}CO, is shown in red. The typical uncertainty per pixel in the observed spectrum is denoted by the error bar (1σ) on the upper left. **b**, A zoom-in over the 2.34–2.40 μm spectral region, centred on the ^{13}CO bandhead. Specific opacity from ^{13}CO is located where the reduced model without ^{13}CO (in red) is higher than the observed spectrum. **c**, The residuals (spectrum minus best-fit models, with the residuals of the reduced model in red) revealing the Brγ emission feature at 2.166 μm and Na I absorption lines. **d**, Observational residuals in red are compared with the ^{13}CO absorption model in black (the difference between the best-fit full model minus the same model with the ^{13}CO opacity removed), revealing the similarity between the observations and models. **e**, CCFs between observational residuals and the ^{13}CO model, as shown in black. The dashed line shows the autocorrelation of the ^{13}CO model, scaled to the peak of the CCF.

substantially better fit in terms of χ^2 (Extended Data Fig. 1c) as a result of the additional ^{13}CO opacity.

To qualitatively reveal the signature, we compare the observational residuals (that is, the observed spectrum with the best-fit reduced model subtracted off) to the noise-free template of the ^{13}CO signal (that is, the best-fit full model subtracted by the same full model with the ^{13}CO abundance set to zero). The observational residuals follow the expected ^{13}CO signal, especially the dip caused by the ^{13}CO bandheads and well aligned individual lines (Fig. 1d), which indicates the presence of ^{13}CO in the data. We also cross-correlated the residuals with the ^{13}CO model (Fig. 1e). The cross-correlation function (CCF) between the observation and model follows the autocorrelation function (ACF) of the model well. The broad feature in the CCF (and ACF) reflects the effect of ^{13}CO bandheads, and the peak at zero radial velocity co-adds the individual lines of the ^{13}CO signal.

In terms of the significance of the ^{13}CO detection, comparing the Bayesian evidence (Z) of the reduced model with the full model allows us to assess the extent to which the model including ^{13}CO is favoured by the observations. In the Bayesian model comparison, the Bayes factor B_m (calculated by the ratio of Z) is used as a proxy for the posterior odds ratio between two alternative models[21]. As a result, the Bayes factor between two models is $\ln(B_m) = \Delta\ln(Z) = 18$, meaning that the observation favours the full model (including ^{13}CO) at a significance level of $>6\sigma$.
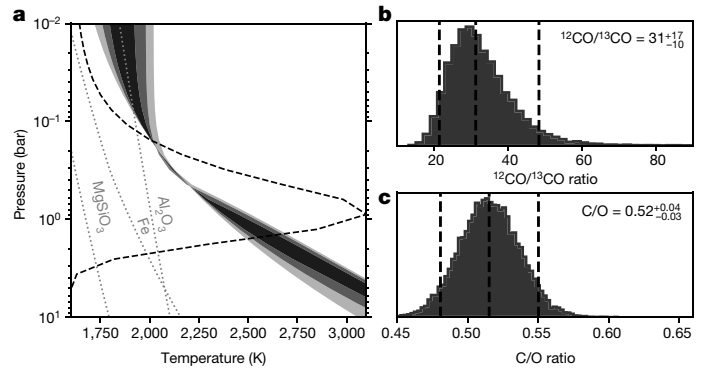

Fig. 2 | Spectral retrieval results. a, The retrieved temperature–pressure profile. The shaded regions with decreasing grey scale show 1σ, 2σ and 3σ temperature uncertainty envelopes, respectively. The grey dotted lines represent the condensation curves of three potential cloud species. The black dashed line shows the flux average of the emission contribution function. **b**, Posterior distribution of CO isotopologue abundance ratio ^{12}CO/^{13}CO. The vertical dashed lines denote the 5%, 50% and 95% quantiles (90% uncertainties) of the distribution. **c**, Posterior distribution of carbon-to-oxygen ratio C/O. The central values and their 90% uncertainties are given in the top right corner.

The central values of the inferred parameters and their 90% uncertainties from the atmospheric retrieval are $R_P = 1.82 \pm 0.08\ R_J$, $\log g = 4.51^{+0.34}_{-0.29}$, [Fe/H] $= 0.07^{+0.31}_{-0.18}$, C/O $= 0.52^{+0.04}_{-0.03}$ and ^{12}CO/^{13}CO $= 31^{+17}_{-10}$ (Fig. 2b, c). Hence, while the C/O ratio is measured to be near the solar value, the atmosphere of the planet is observed to be rich in ^{13}CO. The inferred T–P profile and posterior distribution of parameters for both models are shown in Extended Data Fig. 2.

The ^{12}CO/^{13}CO ratio of 31^{+17}_{-10} we infer for TYC 8998 b is lower (2.5σ) than that measured in the local interstellar medium (about 68; refs. [4,5]), with the latter also lower than the ratio of about 89 observed in the Solar System[1], which is partly thought to be the consequence of galactic chemical evolution, and reflects the relative degree of primary to secondary processing in stars[4–6]. Young systems formed in the local environment are expected to inherit the ^{12}C/^{13}C ratio of about 68. However, the measurements of complex carbon-bearing molecules (which formed at low temperature from CO on grains) towards protostars result in a low ^{12}C/^{13}C ratio of about 30, indicating an enhancement of ^{13}CO or ^{13}C in the ice[22,23]. This may be attributed to carbon fractionation processes, including isotopic ion-exchange reactions[8], isotope-selective photodissociation[9] and ice/gas isotopologue partitioning[7]. The isotopic ion-exchange reactions enhance the ^{13}CO abundance in the gas at low temperatures, followed by the freeze-out of CO gas onto the grains to increase the ^{13}CO abundance in the ice[22]. The ice/gas isotopologue partitioning, owing to the slightly different binding energies of the two isotopologues, may contribute to the enrichment of ^{13}CO in the ice, but only in very narrow temperature ranges as shown by laboratory experiments[24]. The isotope-selective photodissociation alters the ^{12}CO/^{13}CO ratios at different layers in circumstellar disks because the self-shielding of the rarer isotopologues kicks in at a deeper layer into the disk[25]. The preferential photodissociation of ^{13}CO generates more atomic ^{13}C, which freezes out onto the ices in the midplane to enrich the ^{13}C in other complex carbon-bearing molecules. Detailed modelling incorporating these fractionation processes in protoplanetary disks suggests that the ^{13}CO in the gas could also be enhanced at intermediate layers[25]. Planets may be able to accrete the ^{13}CO-rich gas from these intermediate layers through vertical accretion[26]. Alternatively, with the warm gas cycling to cold regions through vertical mixing and then freezing out onto grains, the enrichment may be inherited by pebbles and planetesimals forming there.

In this light, we postulate a framework to explain the ^{13}CO-rich atmosphere of TYC 8998 b, and the near-constant ^{13}C abundance in Solar
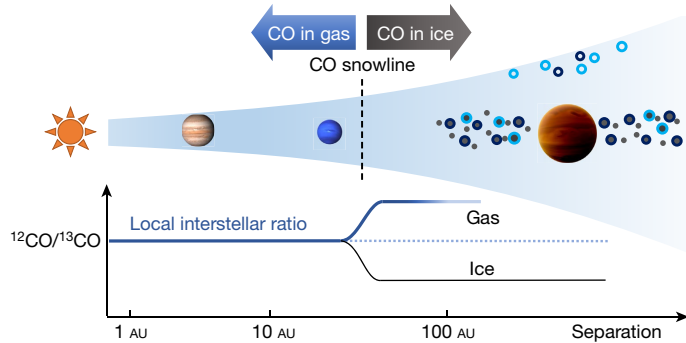
Article

Fig. 3 | Cartoon of the birth environments of planets in a protoplanetary disk. The two planets inside the CO snowline denote Jupiter and Neptune at their current locations, whereas TYC 8998 b is formed far outside this regime, where most carbon is expected to have been locked up in CO ice and formed the main reservoir of carbon in the planet. We postulate that this far outside the CO snowline, the ice was ^{13}CO-rich or ^{13}C-rich through carbon fractionation, resulting in the observed ^{13}CO-rich atmosphere of the planet. A similar mechanism has been invoked to explain the trend in D/H within the Solar System. Future isotopologue measurements in exoplanet atmospheres can provide unique constraints on where, when and how planets are formed.

System objects. It is generally accepted that in the inner parts of a protoplanetary disk, carbon is mostly present in the gas phase as CO, but locked into ices at larger distances, in particular in the disk midplane (Fig. 3). The CO snowline—the transition region between the gaseous and solid phase—is governed by the level of stellar irradiation and is expected to be at around 20 AU for young solar-mass stars[27] such as TYC 8998. The current location of TYC 8998 b at >160 AU is so far out that it has probably formed outside the CO snowline. This implies that it has accreted the bulk of its carbon from ices, which is generally enhanced in ^{13}CO and ^{13}C, as is discussed above, resulting in the observed ^{13}CO-rich atmosphere. Our spectral analysis also points to an atmospheric C/O ratio of $0.52^{+0.04}_{-0.03}$, further suggesting that the planet was indeed formed beyond the CO snowline[19]. Similarly, for other widely separated exoplanets formed outside the CO snowline with substantial ice accretion, we would also expect ^{13}CO-rich atmospheres.

As, in contrast, the Solar System planets are thought to be formed within the CO snowline, we argue that the lack of any substantial enrichment in ^{13}C in their atmospheres is because the bulk of their carbon reservoirs originate from CO gas, not ices. Although Oort cloud comets now reside in the outer Solar System far beyond the snowline, they may have also formed in the inner disk and later been scattered out through the interaction with giant planets[28], therefore exhibiting the same ^{13}C ratios as other objects in the Solar System.

As an analogy of ^{13}CO enrichment through ice accretion, the deuterium-to-hydrogen ratios (D/H) of Uranus and Neptune are found to be enhanced compared with Jupiter, attributed to an increasing contribution from accretion of HDO-rich ices beyond the water snowline[29]. With the caveat that carbon fractionation is orders of magnitude smaller than deuterium fractionation, it could still result in a ^{13}C enrichment of a factor of two. For a further understanding of the role of carbon fractionation in planet formation, it will be important to obtain a quantitative assessment of the effects through detailed disk modelling. Future measurements of exoplanet $^{12}C/^{13}C$ (and D/H) ratios[18,30] can provide an exciting way to constrain when, where and how planets are formed.

Online content

Any methods, additional references, Nature Research reporting summaries, source data, extended data, supplementary information, acknowledgements, peer review information; details of author contributions and competing interests; and statements of data and code availability are available at https://doi.org/10.1038/s41586-021-03616-x.

1. Clayton, D. D. & Nittler, L. R. Astrophysics with presolar stardust. *Annu. Rev. Astron. Astrophys.* **42**, 39–78 (2004).
2. Wilson, T. L. & Matteucci, F. Abundances in the interstellar medium. *Astron. Astrophys. Rev.* **4**, 1–33 (1992).
3. Woods, P. M. & Willacy, K. Carbon isotope fractionation in protoplanetary disks. *Astrophys. J.* **693**, 1360–1378 (2009).
4. Langer, W. D. & Penzias, A. A. $^{12}C/^{13}C$ isotope ratio in the local interstellar medium from observations of $^{13}C^{18}O$ in molecular clouds. *Astrophys. J.* **408**, 539–547 (1993).
5. Milam, S. N., Savage, C., Brewster, M. A., Ziurys, L. M. & Wyckoff, S. The $^{12}C/^{13}C$ isotope gradient derived from millimeter transitions of CN: the case for galactic chemical evolution. *Astrophys. J.* **634**, 1126–1132 (2005).
6. Prantzos, N., Aubert, O. & Audouze, J. Evolution of the carbon and oxygen isotopes in the Galaxy. *Astron. Astrophys.* **309**, 760–774 (1996).
7. Smith, R. L., Pontoppidan, K. M., Young, E. D. & Morris, M. R. Heterogeneity in $^{12}CO/^{13}CO$ abundance ratios toward solar-type young stellar objects. *Astrophys. J.* **813**, 120 (2015).
8. Langer, W. D., Graedel, T. E., Frerking, M. A. & Armentrout, P. B. Carbon and oxygen isotope fractionation in dense interstellar clouds. *Astrophys. J.* **277**, 581–604 (1984).
9. Bally, J. & Langer, W. D. Isotope-selective photodestruction of carbon monoxide. *Astrophys. J.* **255**, 143–148 (1982).
10. Bohn, A. J. et al. The Young Suns Exoplanet Survey: detection of a wide-orbit planetary-mass companion to a solar-type Sco–Cen member. *Mon. Not. R. Astron. Soc.* **492**, 431–443 (2020).
11. Pecaut, M. J. & Mamajek, E. E. The star formation history and accretion-disc fraction among the K-type members of the Scorpius–Centaurus OB association. *Mon. Not. R. Astron. Soc.* **461**, 794–815 (2016).
12. Bohn, A. J. et al. Two directly imaged, wide-orbit giant planets around the young, solar analog TYC 8998–760–1. *Astrophys. J.* **898**, L16 (2020).
13. Eisenhauer, F. et al. SINFONI—integral field spectroscopy at 50 milli-arcsecond resolution with the ESO VLT. In *Proc. SPIE* Vol. 4841 (eds Iye, M. & Moorwood, A. F.M.) 1548–1561 (SPIE, 2003).
14. Bonnet, H. et al. First light of SINFONI at the VLT. *Messenger* **117**, 17–24 (2004).
15. van Holstein, R. G. et al. A survey of the linear polarization of directly imaged exoplanets and brown dwarf companions with SPHERE-IRDIS. First polarimetric detections revealing disks around DH Tau B and GSC 6214–210 B. *Astron. Astrophys.* **647**, A21 (2021).
16. Mollière, P. et al. petitRADTRANS. A Python radiative transfer package for exoplanet characterization and retrieval. *Astron. Astrophys.* **627**, A67 (2019).
17. Buchner, J. et al. Astrophysics X-ray spectral modelling of the AGN obscuring region in the CDFS: Bayesian model selection and catalogue. *Astron. Astrophys.* **564**, A125 (2014).
18. Mollière, P. & Snellen, I. A. G. Detecting isotopologues in exoplanet atmospheres using ground-based high-dispersion spectroscopy. *Astron. Astrophys.* **622**, A139 (2019).
19. Öberg, K. I., Murray-Clay, R. & Bergin, E. A. The effects of snowlines on C/O in planetary atmospheres. *Astrophys. J.* **743**, L16 (2011).
20. Mollière, P. et al. Retrieving scattering clouds and disequilibrium chemistry in the atmosphere of HR 8799e. *Astron. Astrophys.* **640**, A131 (2020).
21. Benneke, B. & Seager, S. How to distinguish between cloudy mini-Neptunes and water/volatile- dominated super-Earths. *Astrophys. J.* **778**, 153 (2013).
22. Jørgensen, J. K. et al. The ALMA Protostellar Interferometric Line Survey (PILS). *Astron. Astrophys.* **595**, A117 (2016).
23. Jørgensen, J. K. et al. The ALMA-PILS survey: isotopic composition of oxygen-containing complex organic molecules toward IRAS 16293–2422B. *Astron. Astrophys.* **620**, A170 (2018).
24. Acharyya, K., Fuchs, G. W., Fraser, H. J., van Dishoeck, E. F. & Linnartz, H. Desorption of CO and O_2 interstellar ice analogs. *Astron. Astrophys.* **466**, 1005–1012 (2007).
25. Miotello, A., Bruderer, S. & van Dishoeck, E. F. Protoplanetary disk masses from CO isotopologue line emission. *Astron. Astrophys.* **572**, A96 (2014).
26. Cridland, A. J., Bosman, A. D. & van Dishoeck, E. F. Impact of vertical gas accretion on the carbon-to-oxygen ratio of gas giant atmospheres. *Astron. Astrophys.* **635**, A68 (2020).
27. Qi, C. et al. Imaging of the CO snow line in a solar nebula analog. *Science* **341**, 630–632 (2013).
28. Morbidelli, A., Levison, H. F., Tsiganis, K. & Gomes, R. Chaotic capture of Jupiter's Trojan asteroids in the early Solar System. *Nature* **435**, 462–465 (2005).
29. Feuchtgruber, H. et al. The D/H ratio in the atmospheres of Uranus and Neptune from Herschel-PACS observations. *Astron. Astrophys.* **551**, A126 (2013).
30. Morley, C. V. et al. Measuring the D/H ratios of exoplanets and brown dwarfs. *Astrophys. J.* **882**, L29 (2019).

Methods

Observations and data analysis

We observed TYC 8998 b on two nights, 5 and 19 June 2019, using SINFONI[13,14] installed at the Cassegrain focus of UT3 of the Very Large Telescope of the European Southern Observatory (ESO) at Cerro Paranal in Chile, under the ESO programme 2103.C-5012(C) (principal investigator, A.J.B.). The observations were performed in the K-band (1.95–2.45 μm), providing a spectral resolving power of about 4,500. The spatial pixel scale is 0.025″ per image slice; therefore, 32 slices in total amount to a field of view (FOV) of 0.8″. Both the primary star and the planet c are outside the FOV (Extended Data Fig. 1). As a result of the large planet–star separation (about 1.7″) and the planet-to-star contrast (magnitude difference of about 6.4)[10], the starlight contamination is small. We obtained 2 × 24 science frames with a number of detector integrations of 2 and an exposure time of 150 s each. The observations were performed in pupil-stabilized mode. During the first night, the airmass ranged from 1.31 to 1.34, the seeing varied from 0.81″ to 2.63″, and the atmospheric coherence time reached 12 ms with the intervention by clouds. Given the unstable atmospheric conditions on the first night, a second night of observation was performed, delivering a seeing ranging from 0.51″ to 1.07″ at an airmass between 1.31 and 1.41 and a coherence time between 2.4 ms and 9.1 ms. During each night, we took three frames of the sky before, during and after the science frames with the same exposure setup. In addition to the science target, one featureless B-type standard star was observed each night, HIP 57861 and HIP 72332, respectively, serving for telluric and spectrophotometric calibration.

The raw data were first reduced using the SINFONI pipeline to correct for bias, flat fielding, sky background and bad pixels. Then we obtained the intermediate two-dimensional data products, which are composed of 32 vertical strips, each representing the spectra taken over an individual slitlet with its own wavelength solution. The target spectrum shows as vertical trails on slitlet images. For each science exposure, we extract the target spectrum from the intermediate two-dimensional frame. We focus our analysis on the brightest four slitlet images, where the spectrum was extracted using the optimal extraction algorithm[31]. This algorithm accounts for background (including the starlight contamination) and automatically rejects outliers caused by bad pixels and cosmic rays, and delivers an optimal signal-to-noise ratio (SNR). We subsequently obtained four target spectra for every science exposure. All the spectra were then linearly interpolated to a common wavelength grid and optimally combined to form a combined spectrum for each night. During the process, we discarded two frames taken on the first night, the data quality of which was too low to clearly identify the target in the data (using a threshold of three times the background noise level) as a result of the poor atmospheric conditions.

The broad-band shapes of the final spectra per night obtained above require cautious calibration. First, the efficiency of the instrument + telescope varies with wavelength. This effect can be corrected by comparing the observed spectral shape of the standard star to its theoretical spectrum. For the standard stars on the first and second nights, we used PHOENIX stellar models[32] with an effective temperature of 13,500 K and 10,800 K, respectively[33,34]. As the observed standard star spectra are firmly in the Rayleigh–Jeans regime, potential uncertainties in effective temperature have only marginal effects on the spectral slope. Second, atmospheric dispersion affects the overall spectral shape differently for different slitlets. The optimal extraction method we adopted can further aggravate this bias as different weights were assigned to slitlets when combining the spectra. To determine the most accurate spectral shape, we extracted spectra again while avoiding weighting. We started from the data cubes reconstructed by the SINFONI pipeline, and took a circular aperture of about five times the full-width at half-maximum to sum up the flux at each wavelength, ensuring that all the flux from the object was included. This plain extraction method was performed on the target as well as standard stars on both nights. In this way, we

derived spectra for the target that have a lower SNR but a more accurate spectral shape. The broad-band shape of this spectrum for each night was then applied to the optimally extracted spectrum by fitting a second-order polynomial to the division between both spectra. After the spectrophotometric correction, the shape of the combined spectra for the two nights differs by about 2% between 2.1 μm and 2.4 μm.

We used the ESO sky software tool Molecfit[35] v3.0.1 to perform telluric corrections on the final spectra of each night. The tool uses a line-by-line radiative transfer model to derive telluric atmospheric transmission spectra that can be fitted to observations. For telluric model fitting, we removed a preliminary planetary model from the observed spectrum to minimize effects from the planetary spectrum on the telluric features. The fitting wavelength region is 2.19–2.43 μm, which contains the majority of strong telluric lines caused by methane (CH_4) and H_2O in Earth's atmosphere. Molecfit accounted for the molecular abundances, instrument resolution, continuum level and wavelength solution that best fit the observations. The atmospheric transmission model for the entire wavelength range was then derived based on the best-fit parameters. Subsequently, the telluric model was removed from the combined spectrum to obtain the telluric-corrected spectrum. However, the correction is not perfect, resulting in artefacts at the red end of the spectra. The wavelength region beyond 2.4 μm, not important for our goals, is therefore masked in further analysis.

After telluric removal, we combined the spectra of both nights into one master spectrum. We noted that the spectrum of the first night turned out to be of lower signal to noise than that of the second night, as expected from the observational conditions. We shifted the two spectra to the planetary rest frame and weighted-combined them by SNR squared. The SNR of each spectrum was measured by the standard deviation of the residuals (that is, the observation minus the model spectrum generated by retrieval fitting) in the wavelength range from 2.35 μm to 2.4 μm. The master spectrum was finally scaled to the photometric flux of 8.8×10^{-16} W m^{-2} μm^{-1} at 2.25 μm (ref. [10]). In this way, we obtained a final master spectrum of the companion shown in Fig. 1, with an SNR of about 50 near 2.2 μm and about 0 at the red end. We note that the uncertainty per wavelength step is almost constant along the wavelengths and independent of the flux of the object because the observations are read-noise limited. The red end of the spectrum, therefore, has lower SNR because of the lower object flux level and strong telluric absorption.

Atmospheric retrieval model

For our atmospheric retrieval, we performed a Bayesian analysis using the radiative transfer tool pRT[16], connected to the nested sampling tool PyMultiNest[17], which is a Python wrapper of the MultiNest method[36]. To model the temperature structure of the planet atmosphere, we consider two classes of parameterization of the T–P profile: the analytical and flexible model. The first temperature model involves analytical solutions for self-luminous atmospheres assuming a grey opacity. We set the temperature according to Eddington approximation: $T(\tau)^4 = 0.75T_{int}^4(2/3 + \tau)$, where the optical depth τ is linked to the pressure by $\tau = \delta P^\alpha$, with δ and α as free parameters. We defined P_{phot} as the pressure where $\tau = 1$. Hence, $\delta = P_{phot}^{-\alpha}$. This temperature model therefore has three free parameters, T_{int}, α and P_{phot}, with T_{int} as the effective temperature. The Eddington solution leads to an isothermal upper atmosphere. Although this seems unrealistic, the model still works well because the medium-resolution observations barely probe that high up in the atmosphere. At low altitudes, the atmosphere transitions to convective, where we force the temperature gradient onto a moist adiabat.

In the flexible temperature model, we focus on the temperature from 0.01 bar to 10 bar, where the contribution function of the observed spectrum peaks. The temperature outside this range is considered to be isothermal. We set four temperature knots spaced evenly on a log-scale pressure within 0.02 bar to 5 bar. The T–P profile is obtained

by spline interpolation of the temperature knots in the log space of pressure. There is no physical reasoning behind this T–P profile, therefore imposing fewer prior constraints on the solution.

The chemistry model used in our retrievals is detailed in ref. [20]. In short, the chemical abundances are determined via interpolation in a chemical equilibrium table using pressure P, temperature T, carbon-to-oxygen ratio C/O and metallicity [Fe/H] as inputs. Then pRT computes synthetic emission spectra using temperature, chemical abundances and surface gravity as inputs.

We tested the retrieval framework to ensure parameters can be correctly recovered by using synthetic spectra. Using the forward model presented above, we generated a mock spectrum at 2.1–2.45 μm, with a spectral resolution of 4,500. The flux error was set to be constant, leading to an SNR of around 50 at 2.2 μm, which is similar to that in the master spectrum. The mock spectrum was then perturbed by random noise generated according to this uncertainty in flux. We were able to recover all parameters within a 1σ interval, validating the capability of the retrieval model.

Retrievals on the TYC 8998 b spectrum

We set up the retrieval model using the analytical T–P profile, with eight free parameters, R_P, log g, [Fe/H], C/O, T_{int}, α, P_{phot} and $^{12}CO/^{13}CO$. The priors of these free parameters are listed in Extended Data Table 1. In the full model, we included ^{12}CO, H_2O, CH_4, ammonia (NH_3) and the isotopologue ^{13}CO as line opacity species, and the collision-induced absorption of H_2–H_2 and H_2–He. As for the reduced model, we removed ^{13}CO from the opacity sources. We used the line-by-line mode of pRT to calculate the emission spectra at high spectral resolution. To speed up the calculation, we took every fifth point of opacity tables with $\lambda/\Delta\lambda \approx 10^6$. This sampling procedure, which has been benchmarked against the full tables, shows negligible effects on the synthetic spectra and retrieval results. The synthetic high-resolution spectra were convolved with a Gaussian kernel to match the resolving power of the instrument ($R \approx 4,500$), then binned to the wavelength grid of the master spectrum, and scaled to the observed flux according to R_P and distance of the target.

In addition, as we noted above, there exists up to 2% discrepancy in terms of the broad-band spectral shape between the two nights of observations. Therefore, before comparing the synthetic model spectra to the observation, we multiplied the models by a linear slope spanning from $1 - f_{slope}$ to $1 + f_{slope}$ in the wavelength range from 2.1 μm to 2.4 μm, where we introduced the slope correction factor f_{slope} as a nuisance parameter to marginalize the uncertainty in the spectral shape. The retrieval process was performed by PyMultiNest, which uses 4,000 live points to sample the parameter space and derives the posterior abundances of the fit. We ran MultiNest in 'importance nested sampling' mode with a constant efficiency of 5%. The outcome is shown in Extended Data Fig. 2. We also used the flexible T–P profile to consolidate the retrieval results. The inferred parameters are found to be robust for different T–P model setups.

The retrieved value of log g should be treated with caution, because we note that any small changes in the wavelength coverage of the fitting or the broad-band shape of the spectrum can result in notably different values. As also indicated in other retrieval studies[37], CO and H_2O features in the K-band are not very sensitive to log g. Free retrievals in the K-band alone are therefore unable to place robust constraints on the surface gravity and hence the planet mass. We also run retrievals with prior constraint on the planet mass. The solution converges to a lower surface gravity and the same isotopologue ratio, suggesting that the inaccurate log g does not affect the inference of the $^{12}CO/^{13}CO$ ratio.

We compared the Bayesian evidence (Z) of the reduced model with the full model (Extended Data Fig. 1c), the difference of which is related to the Bayes factor B_m that translates to a frequentist measure[21] of more than 6σ significance of the ^{13}CO detection. Although the evidence is dependent on the prior of the ^{13}CO abundance (Extended Data Table 1),

we noted that increasing the prior range of log($^{13}CO/^{12}CO$) from (−12, 0) to (−20, 0) did not lead to a notable change in the final evidence, and both of the priors are much broader than the ratio that one would expect in reality.

Effects of clouds

Clouds are ubiquitous in planetary atmospheres and can have an important role in the interpretation of spectra. We investigated their potential effects on the ^{13}CO measurement by including clouds in the retrieval models. We used the cloud model detailed in ref. [19], which introduced four additional free parameters: the vertical eddy diffusion coefficient K_{zz}, the settling parameter f_{sed}, the width of the log-normal particle size distribution σ_g and the mass fraction of the cloud species at the cloud base log X. The temperature of TYC 8998 b is too high to form magnesium- and iron-bearing condensates in the atmosphere. We therefore considered a more refractory species, aluminium oxide (Al_2O_3), as the source of cloud opacity[38]. After testing cloudy models, we found the solution converged to cloud-free atmospheres, and the inferred parameter values remained unaffected, because the atmospheric temperature (Fig. 2a) is too warm to form optically thick clouds that could make a substantial impact on the spectrum. Therefore, we did not include clouds in our nominal models.

Constraining mass accretion rate

The Brγ emission line (Fig. 1) provides constraints on the mass accretion rate of the planet. We measured a Brγ line flux of 7.6 (± 0.9) × 10^{-18} W m^{-2}, and a line luminosity $L_{Brγ}$ compared with the solar luminosity $L_{\odot}$ of log($L_{Brγ}/L_{\odot}$) of −5.7 ± 0.5, from which we estimated the accretion luminosity log($L_{acc}/L_{\odot}$) to be −2.7 ± 1.3 using the linear correlation given by ref. [39]. Combining this with the retrieved values of radius and surface gravity, we derived a mass accretion rate of $10^{-9.4±1.3} M_{\odot}$ yr^{-1}.

Additional assessments of the reliability of ^{13}CO detection in TYC 8998 b

We further assess the reliability of the ^{13}CO detection in several ways. We study the ^{13}CO signal for the individual nights and that from the first and second bandheads separately, and investigate the impact of inaccurate telluric line removal and the effects of possible other opacity sources. In addition, we show that for an easier accessible, nearby, isolated brown dwarf, archival spectroscopy data of the same ^{13}CO features at higher spectral resolving power show a strong signal—as expected from our TYC 8988 b observations (albeit with a more typical $^{12}CO/^{13}CO$ ratio).

Analysis on data of individual nights and bandheads

To assess whether the ^{13}CO signal is present on both nights, we performed the retrieval and cross-correlation analyses as detailed above for each night separately. The retrieval results are shown in Extended Data Fig. 3. ^{13}CO is detected on both nights but at a lower significance, as expected. The derived constraints on $^{12}CO/^{13}CO$ are consistent with each other. There is around 2% difference in the slope correction factor f_{slope} on the two nights, as already noted in the spectral calibration above. This probably contributes to the slight discrepancies in the derived values for log g and C/O. The CCFs are shown in Extended Data Fig. 4, also indicating that ^{13}CO is detected on both nights individually, albeit at lower significance.

We also investigated whether the two bands of ^{13}CO, starting at 2.345 μm and 2.374 μm, can both be detected individually. We examined this by separating the wavelength region into two parts, 2.34–2.37 μm and 2.37–2.40 μm, then calculating the cross-correlation in each part. Before the cross-correlation, the residuals were high-pass filtered using a Gaussian kernel with a width of 3 nm to remove the low-frequency variation in residuals and enhance the signal. The low-frequency variation, especially apparent in the second part of the data, introduces broad-band shape in the CCF, which suppresses the signal. The filtered residuals are shown in Extended Data Fig. 4c, and the cross-correlation

results in Extended Data Fig. 4d. The CCF for both bands show peaks at zero velocity, while the signal from the second band is less significant. We argue that although the expected absorption from the two bands is similar, the signal to noise of the spectral data at the 2.374-μm bandhead is lower due to the stronger telluric absorption in this region. This is highlighted in Extended Data Fig. 5a, showing the telluric transmission spectrum, observational residuals from the reduced model (without ^{13}CO), and the ^{13}CO model. We believe that it is for this reason that the ^{13}CO signal from the second bandhead is not as significant as from the first bandhead.

Impact of telluric absorption

Extended Data Fig. 5b shows the CCF between the ^{13}CO model and the telluric line spectrum, demonstrating no evident signal. It indicates that the observed ^{13}CO signal is not caused by any under- or overcorrection of telluric lines.

Other potential opacity sources

In the retrieval models, we include the major molecular opacity sources (CO, H_2O, CH_4 and NH_3) that have a role in the K-band. We inspected other potential absorbers given the expected temperature, including carbon dioxide (CO_2), hydrogen cyanide (HCN) and acetylene (C_2H_2). None of them shows notable features at the same wavelength region as ^{13}CO. Moreover, we performed retrieval analysis to marginalize over these absorbers. Adding these molecules to the retrieval model does not change the inferred value of any parameter. Therefore, it is not plausible that the detected ^{13}CO feature is caused by these molecules.

Archival reference data of the young brown dwarf 2M0355

To boost confidence in the detection of ^{13}CO in TYC 8998 b, we analysed archival data of the young brown dwarf 2M0355 (ref. [40]). This object resembles in several ways a young super-Jupiter like TYC 8998 b, but as it is isolated, and located nearby at 8 parsec, it is spectroscopically much more accessible. From our ^{13}CO detection in TYC 8988 b, it is expected that ^{13}CO should be straightforward to see in 2 h of data[41] from the near-infrared echelle spectrograph (NIRSPEC) at the Keck telescope, in particular at a spectral resolving power of $\lambda/\Delta\lambda \approx 27,500$. Our detailed analysis will be presented in a forthcoming publication. Extended Data Fig. 6 shows the spectrum, best-fit model and the ^{13}CO cross-correlation signal, after performing an identical analysis—targeting the same features as our SINFONI data of TYC 8998 b. We retrieve a $^{12}CO/^{13}CO$ isotopologue abundance of around 90–100, similar to the solar value. It will be intriguing to compare measurements between isolated brown dwarfs and exoplanets, revealing the role of the carbon isotopologue ratio as a tracer of planet formation.

Data availability

The data are publicly available from the ESO Science Archive with the programme ID 2103.C-5012(C).

Code availability

The data analysis was performed with custom Python scripts following the standard procedure. The code and reduced spectrum are available from https://gitlab.strw.leidenuniv.nl/yzhang/yses1b-sinfoni. The atmospheric retrieval models use petitRADTRANS, which is available from https://petitradtrans.readthedocs.io/, and the nested sampling tool PyMultiNest, which is available from https://johannesbuchner.github.io/PyMultiNest/.

31. Horne, K. An optimal extraction algorithm for CCD spectroscopy. *Publ. Astron. Soc. Pacif.* **98**, 609–617 (1986).
32. Husser, T.-O. et al. A new extensive library of PHOENIX stellar atmospheres and synthetic spectra. *Astron. Astrophys.* **553**, A6 (2013).
33. Shokry, A. et al. Stellar parameters of Be stars observed with X-shooter. *Astron. Astrophys.* **609**, A108 (2018).
34. McDonald, I., Zijlstra, A. A. & Boyer, M. L. Fundamental parameters and infrared excesses of Hipparcos stars. *Mon. Not. R. Astron. Soc.* **427**, 343–357 (2012).
35. Smette, A. et al. Molecfit: a general tool for telluric absorption correction. *Astron. Astrophys.* **576**, A77 (2015).
36. Feroz, F., Hobson, M. P. & Bridges, M. MultiNest: an efficient and robust Bayesian inference tool for cosmology and particle physics. *Mon. Not. R. Astron. Soc.* **398**, 1601–1614 (2009).
37. Nowak, M. et al. Peering into the formation history of β Pictoris b with VLTI/GRAVITY long-baseline interferometry. *Astron. Astrophys.* **633**, A110 (2020).
38. Wakeford, H. R. et al. High-temperature condensate clouds in super-hot Jupiter atmospheres. *Mon. Not. R. Astron. Soc.* **464**, 4247–4254 (2017).
39. Muzerolle, J., Hartmann, L. & Calvet, N. A Brγ probe of disk accretion in T Tauri stars and embedded young stellar objects. *Astron. J.* **116**, 2965–2974 (1998).
40. Reid, I. N. et al. Meeting the cool neighbors. X. Ultracool dwarfs from the 2MASS all-sky data release. *Astron. J.* **136**, 1290–1311 (2008).
41. Bryan, M. L. et al. Constraints on the spin evolution of young planetary-mass companions. *New Astron.* **2**, 138–144 (2018).

Extended Data Fig. 1 | Schematics of the observations of TYC 8998-760-1 b using SINFONI at the Very Large Telescope. The background image is captured by the SPHERE instrument on the VLT (Credit: ESO/Bohn et al.). The small blue box marks the FOV of SINFONI observations targeting the planet b. Both the host star and planet c are outside the FOV. An example of the wavelength-collapsed image is shown in the enlarged blue box, showing negligible contribution from starlight.

(a)

Full model

Reduced model

(b)

(c)

	Full model	Reduced model
$\ln(Z)$	-479.3	-497.6
Best-fit χ^2	893.7	937.6
$\ln(B_m)$	18 ($\sim 6\sigma$)	-
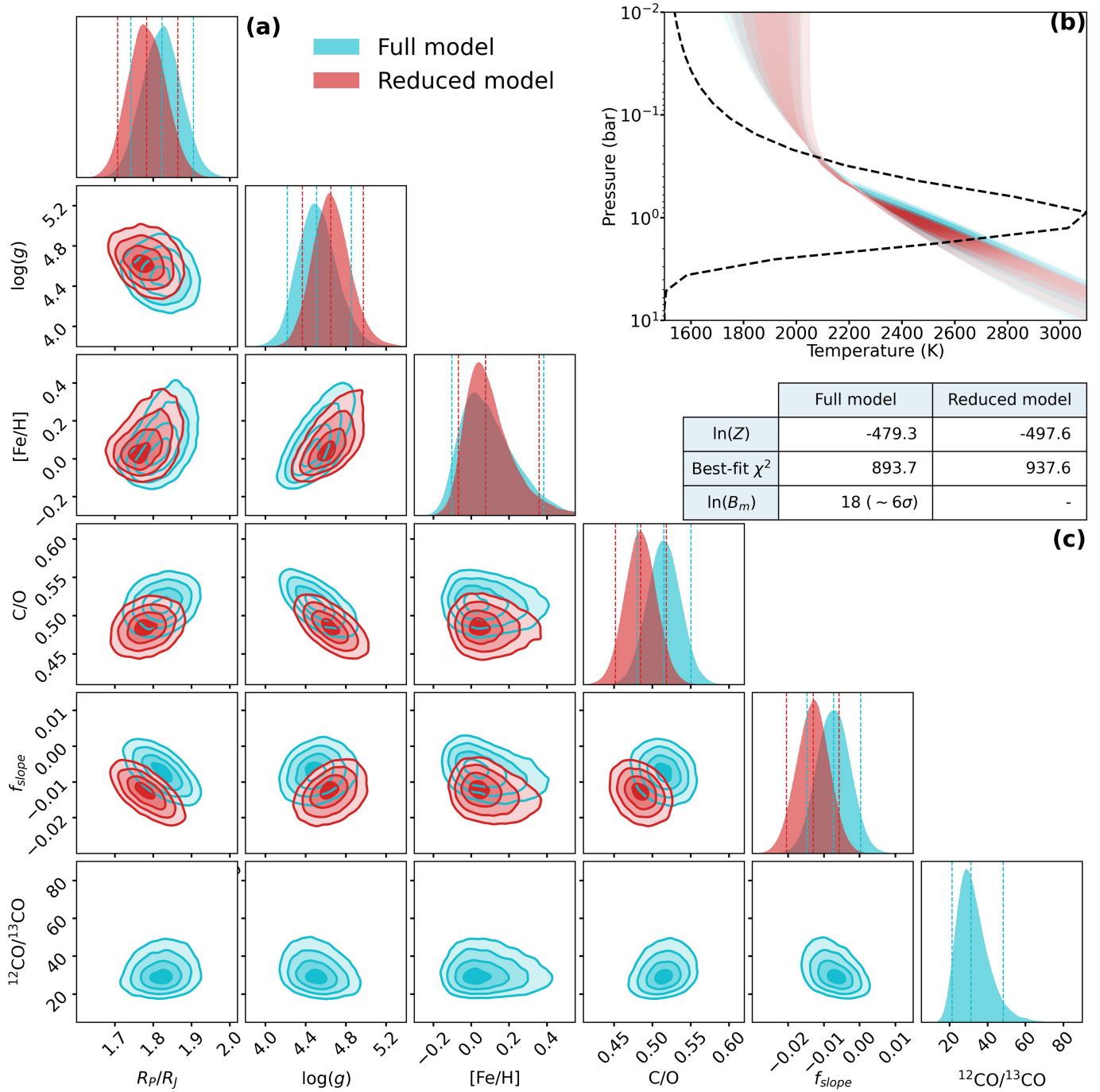
Extended Data Fig. 2 | Posteriors of retrieved parameters. a, Posteriors of the retrieved parameters and temperature structure for the full (cyan) and reduced (red) models. The vertical dashed lines denote the 5%, 50% and 95% quantiles (90% uncertainties) of the distribution. **b**, T–P profile. The shaded regions with decreasing colour saturation show 1σ, 2σ and 3σ temperature uncertainty envelopes, respectively. The black dashed line shows the flux average of the emission contribution function. The opaqueness of the temperature uncertainty envelopes has been scaled by this contribution function. **c**, Fitting statistics of the full and reduced retrieval model, where $\ln(Z)$ and $\ln(B_m)$ represent the logarithm of Bayesian evidence and Bayes factor, respectively.
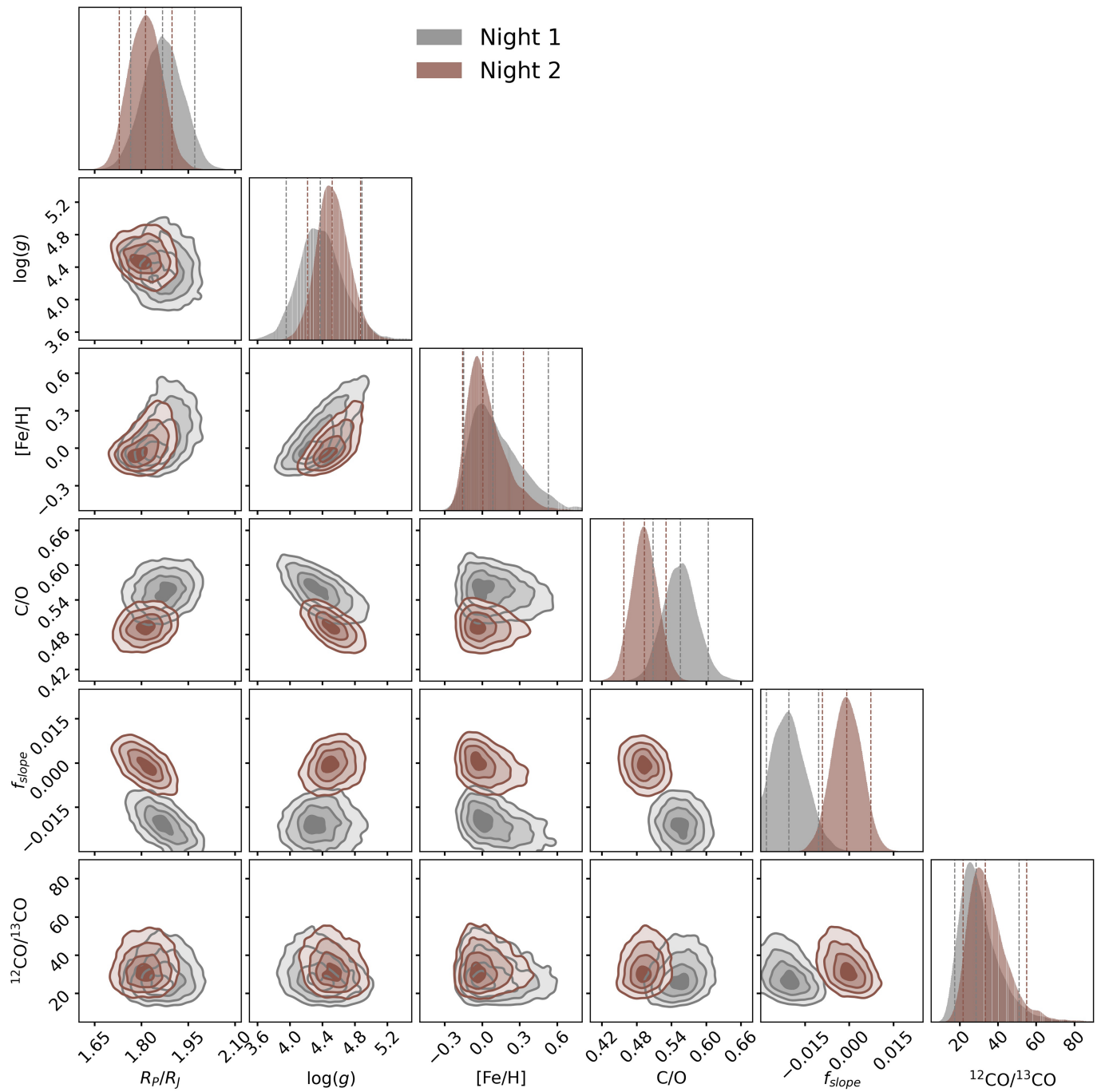
Extended Data Fig. 3 | Posteriors of the retrieved parameters for the data of individual nights. Similar to Extended Data Fig. 2a.
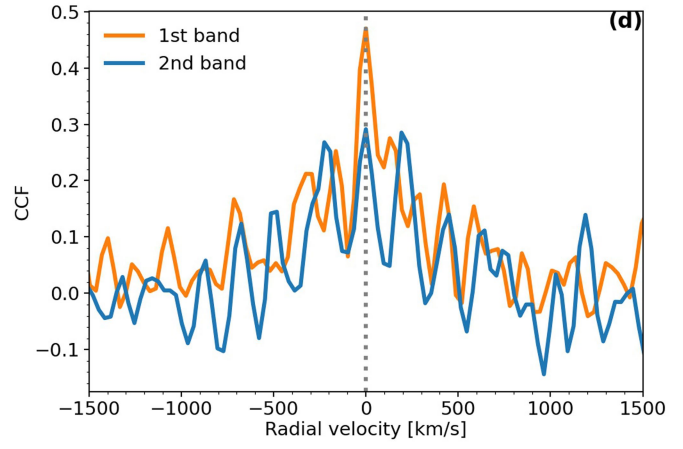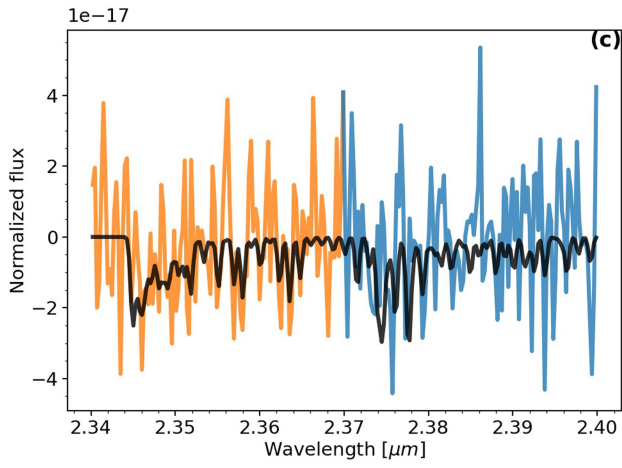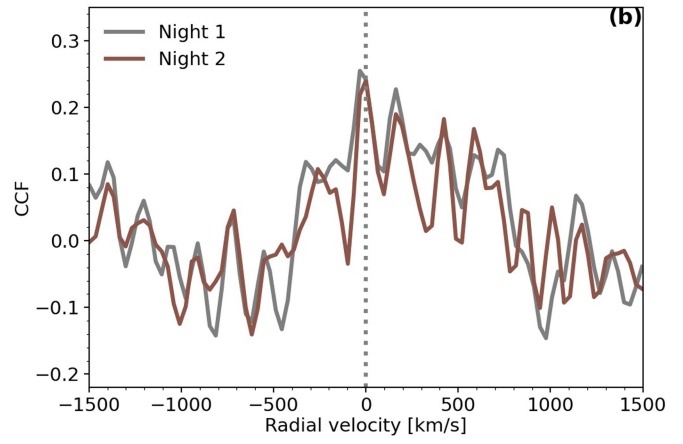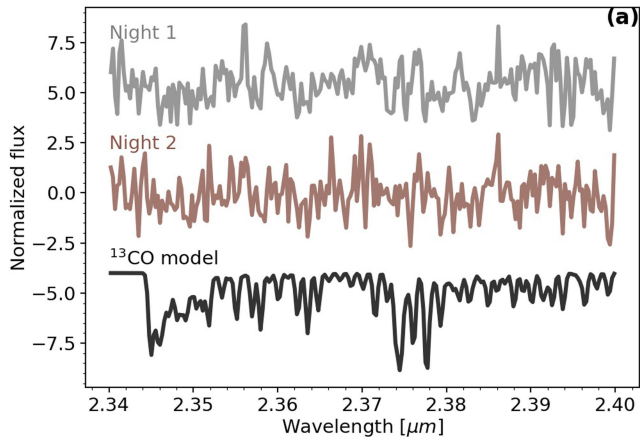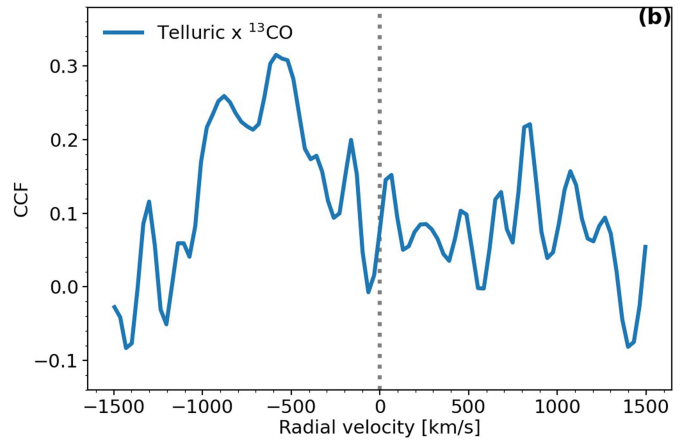
Extended Data Fig. 4 | Cross-correlation signal of ^{13}CO from individual nights and bandheads. a, Observational residuals of the two nights separately. **b**, Cross-correlation signal from the individual nights. **c**, Filtered observational residuals of the two ^{13}CO bandheads separately. **d**, Cross-correlation signal from the individual bandheads.
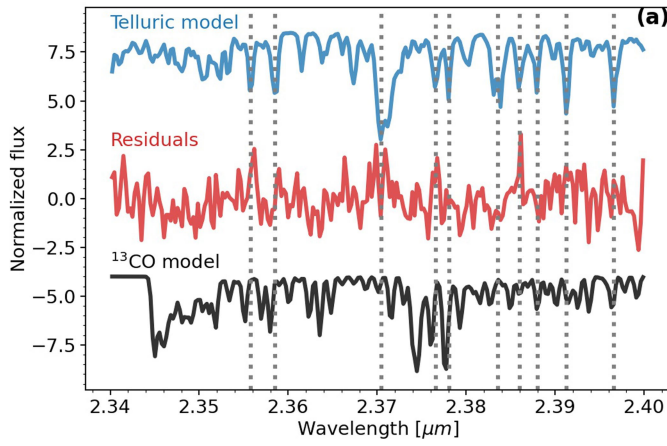
Extended Data Fig. 5 | Impact of telluric absorption lines and cross-correlation signal of ^{13}CO at the extended wavelength region. a, Comparison of the telluric transmission model with residuals. Some noise is attributed to imperfect telluric correction as noted by dotted grey lines. **b**, Cross-correlation function between the telluric model and the ^{13}CO model, showing no correlation between them.
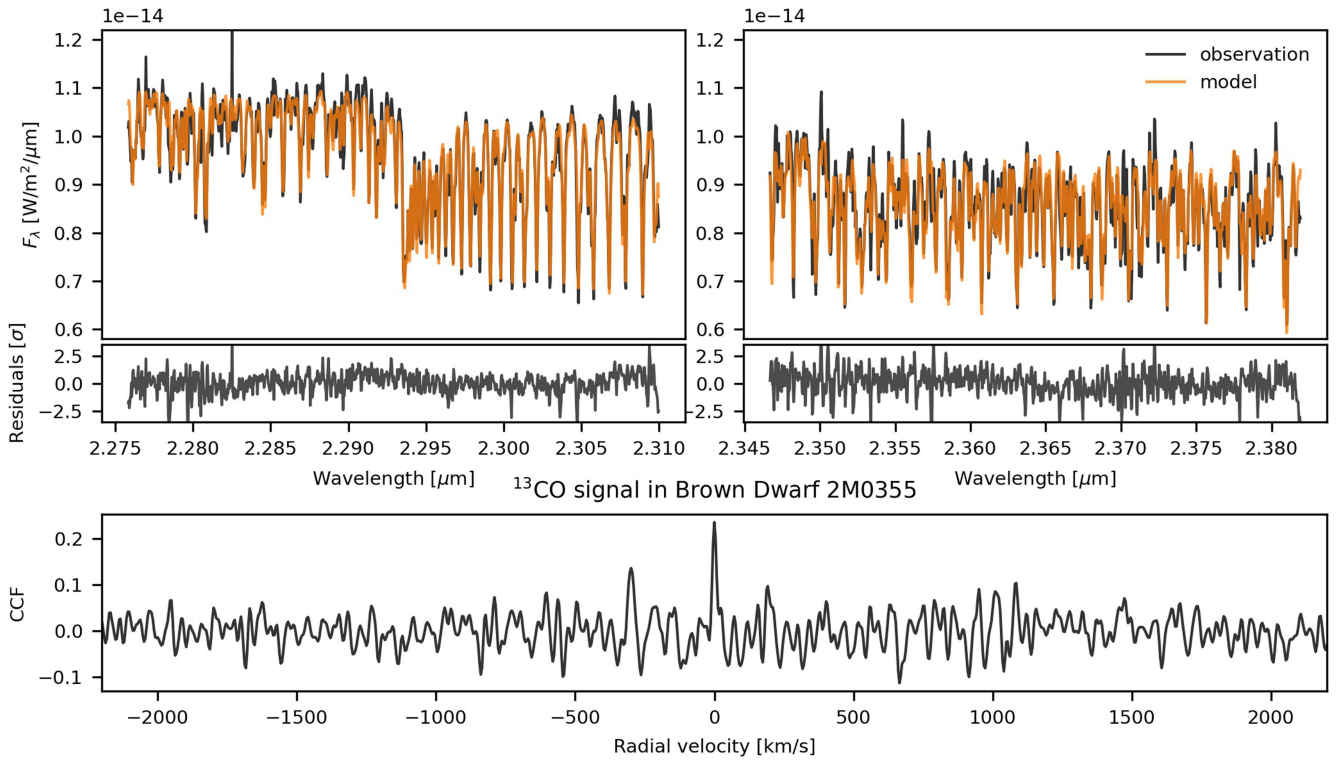
Extended Data Fig. 6 | K-band spectrum of the brown dwarf 2M0355 taken by Keck/NIRSPEC and the cross-correlation signal of ^{13}CO. The black line shows the observed spectrum and the orange line is the best-fit model obtained by retrieval analysis. Bottom: CCF between the ^{13}CO model and observational residuals. The peak at zero velocity clearly shows the detection of ^{13}CO.

Article

Extended Data Table 1 | Priors and inferred posteriors of the TYC 8998 b retrieval

Parameter	Prior	Posterior (90%)
R_P [R_J]	$U(1, 3)$	1.82 ± 0.08
$\log(g)$ [$\log(cm\ s^{-2})$]	$U(2.5, 6)$	$4.51^{+0.34}_{-0.29}$
[Fe/H]	$U(-1.5, 1.5)$	$0.07^{+0.31}_{-0.18}$
C/O	$U(0.1, 1.5)$	$0.52^{+0.04}_{-0.03}$
T_{int} [K]	$U(1000, 3000)$	2174^{+162}_{-150}
α	$U(0.1, 2)$	$0.8^{+0.8}_{-0.2}$
$\log(P_{phot})$ [bar]	$U(-3,2)$	$-0.19^{+0.10}_{-0.29}$
$\log(^{13}CO/^{12}CO)$	$U(-12, 0)$	$-1.49^{+0.16}_{-0.19}$
f_{slope}	$U(-0.05, 0.05)$	-0.007 ± 0.007

$U(a, b)$ represents a uniform distribution ranging from a to b.